The Astrophysical Journal Letters, 947:L1 (9pp), 2023 April 10 https://doi.org/10.3847/2041-8213/acc93f

Pointlike Sources among $z > 11$ Galaxy Candidates: Contaminants due to Supernovae at High Redshifts?

Haojing Yan[1], Lifan Wang[2], Zhiyuan Ma[3], and Lei Hu[4]
[1] Department of Physics and Astronomy, University of Missouri, Columbia, MO 65211, USA; yanhaojing@gmail.com
[2] George P. and Cynthia Woods Mitchell Institute for Fundamental Physics & Astronomy, Texas A&M University, Department of Physics and Astronomy, 4242 TAMU, College Station, TX 77843, USA
[3] Department of Astronomy, University of Massachusetts, Amherst, MA 01003, USA
[4] Purple Mountain Observatory, Chinese Academy of Sciences, No. 10 Yuanhua Road, Qixia District, Nanjing, Jiangsu 210023, People's Republic of China
Received 2023 January 23; revised 2023 March 29; accepted 2023 March 30; published 2023 April 11

Abstract

The recent searches for $z > 11$ galaxies using the James Webb Space Telescope have resulted in an unexpectedly high number of candidate objects, which imply at least 1 order of magnitude higher number density of $z > 11$ galaxies than the previously favored predictions. A question has risen whether there are some new types of contaminants among these candidates. The candidate sample of Yan et al., totaling 87 dropouts, is the largest one, and we notice that a number of these candidates are pointlike. We hypothesize that the point-source dropouts could be supernovae at high redshifts. Further investigation shows that most of their spectral energy distributions indeed can be explained by supernovae at various redshifts from $z \sim 1$ to 15, which lends support to this hypothesis. Attributing such point-source dropouts to supernova contamination cannot eliminate the tension, however, because they only account for ∼10% of the Yan et al. sample. On the other hand, the discovery of "contaminant" supernovae at $z > 3$ will have a series of important implications. Ironically, the existence of supernovae at $z > 10$ would still imply that the previously favored picture of early galaxy formation severely underestimates the global star formation rate density such redshifts. Multiple-epoch JWST imaging will be the simplest and yet the most efficient way to further test this hypothesis.

Unified Astronomy Thesaurus concepts: Galaxy evolution (594); Galaxy formation (595); Early universe (435); Supernovae (1668); Core-collapse supernovae (304); Type Ia supernovae (1728)

1. Introduction

Since its Early Release Observations (ERO), James Webb Space Telescope (JWST) has created a flux of new searches for high-redshift ($z > 11$) candidate galaxies (Bouwens et al. 2022; Castellano et al. 2022; Finkelstein et al. 2022; Harikane et al. 2022; Naidu et al. 2022; Adams et al. 2023; Atek et al. 2023; Donnan et al. 2023; Rodighiero et al. 2023; Yan et al. 2023b, 2023a). The large number of candidates (over a hundred as of this writing) resulted from these studies are incompatible with the previously favored predictions at $z > 11$ (see, e.g., Behroozi et al. 2020; Vogelsberger et al. 2020). The problem is exacerbated by the fact that some of these candidates are much brighter ($m \lesssim 26.5$ mag) than what would be expected for galaxies at such high redshifts (see, e.g., Yan et al. 2023a for a summary). If a significant fraction of these objects are indeed at $z > 11$, we will have severe difficulty in reconciling them with our current picture of galaxy formation in the early universe.

Among all the $z > 11$ candidate samples selected using the early JWST data, the one presented by Yan et al. (2023b, hereafter Y23) is the largest and has attempted to probe the highest redshift range. It was based on the six-band NIRCam images of the nearby galaxy cluster SMACS J0723-73, which were taken as part of the JWST ERO (Pontoppidan et al. 2022). Only half of the field centered on the cluster is boosted by lensing, and the other half is not affected. Their candidates were selected as the dropouts from F150W (60 objects), F200W (15 objects), and F277W (12 objects), respectively, which nominally correspond to $z \approx 12.7$, 17.3, and 24.7, respectively. Such a large number of $z > 11$ candidate objects pose the most severe challenge to the current picture of galaxy formation in the early universe.

Y23 also cautioned that some of their candidates, while having good spectral energy distribution (SED) fits consistent with being at $z > 11$, could still be due to some new types of contaminators that were not encountered previously in high-z searches. We notice that a few of these dropouts are pointlike sources. In the dropout searches at lower redshifts ($z \leqslant 10$), such pointlike sources would be identified as contaminants due to Galactic brown dwarf stars. However, Y23 demonstrated that their colors are inconsistent with brown dwarfs, which can be understood because the broad molecular absorption bands of brown dwarfs do not locate in the wavelength range of our interest. All of this motivates us to consider if any of these point sources could be supernovae (SNe). SNe exhibit a wide range of properties in their SEDs at different evolutionary stages, and they generally have a sharp cutoff at a rest frame $\lesssim$4000 Å postmaximum because of the sudden onset of strong metal line absorption (see Section 3 for details of the SED fits). This raises the possibility that they could become contaminators to high-z searches. In this Letter, we explore such a possibility using the slightly extended dropout sample of Y23. The selection of point sources in this sample is given in Section 2. We study the SN interpretation by carrying out SED fitting to the model SN templates, which is detailed in Section 3. We discuss the implication of our results in Section 4 and conclude with Section 5. All magnitudes quoted are in the AB system. All coordinates are of J2000.0 Equinox.

We adopt the following cosmological parameters: $\Omega_M = 0.27$, $\Omega_\Lambda = 0.73$, and $H_0 = 71$ km s^{-1} Mpc^{-1}.

2. Point Sources among Dropouts

The JWST ERO NIRCam observations of SMACS 0723-73 were done in six broad bands, namely, F090W, F150W, and F200W in the "short wavelength" (SW) channel and F277W, F356W, and F444W in the "long wavelength" (LW) channel. Hereafter we refer to the magnitudes in these bands as m_{090}, m_{150}, m_{200}, m_{277}, m_{356}, and m_{444}, respectively. Y23 selected $z > 11$ candidates using the standard "dropout" technique (Steidel et al. 1995) to identify the characteristic Lyman-break signature in their SEDs. They adopted the color decrement of $\geqslant$0.8 mag and signal-to-noise ratio (S/N) $\leqslant 2$ (i.e., nondetections) in the veto band(s). For reference, when the break moves to halfway of the drop-out band, the color decrement is $\sim$0.75 mag if the SED is flat in f_ν. In total, they have selected 60 F150W dropouts, 15 F200W dropouts, and 12 F277W dropouts, respectively. This is the largest high-z dropout sample to date.

Our visual inspection of these dropouts suggests that a number them are pointlike. To confirm that they are indeed point sources, we carried out further investigations. The NIRCam image stacks used in Y23 were all produced at the pixel scale of 0.″06 (hereafter "60 mas"), which was chosen to match the native pixel scale of F356W and to optimize the detection of faint objects. However, such a scale is not ideal for our purposes here because it undersamples the three SW band (F090W, F150W, and F200W) passbands, which have better resolutions (as much as $\sim 2\times$) than the three LW bands (F277W, F356W, and F444W). Therefore, we created a new version of images at the pixel scale of 0.″03 (hereafter "30 mas") to identify point sources. Thanks to the sufficient dithers employed by this set of observations, the 30 mas stacks are critically (Nyquist) or better sampled in SW and oversampled in LW. We also updated the reference files to the JWST calibration reference data system (CRDS) context "jwst_1008.pmap," which incorporates the best flux zero-point calibration as of this writing. To take the full advantage of the wavelength coverage of the NIRCam data, we extended the Y23 dropout sample to include F356W dropouts. These were selected from a source catalog constructed in a similar way as in Y23, with the difference that the F444W images were used for the source detection and aperture definition. A legitimate F356W dropout must have an S/N $\geqslant 5$ in F444W, satisfy $m_{356} - m_{444} \geqslant 0.8$ mag, and have an S/N $\leqslant 2$ in all the veto bands (i.e., those bluer than F356W). To ensure sufficient S/N in evaluating their sizes, we truncated the F356W dropouts to $m_{444} \leqslant 29.0$ mag. As it turns out, there is only one such F356W dropout left after this truncation.

To identify the point sources among the dropout sample, we first singled out those that appears to be pointlike by visual inspection in F200W, F277W, F356W, and F444W. We then fitted a 2D Gaussian profile to these objects to check whether they had FWHM values consistent with expectations for point sources seen by the NIRCam. As the in-flight NIRCam PSFs have not yet been fully characterized in this early stage of the JWST mission, we took an empirical approach, which is detailed in the Appendix. Briefly, we selected high-S/N point sources in the field based on the diagnostics used by the PSFEx software tool (Bertin 2011), determined the average FWHM values and the dispersions in the four aforementioned bands, and compared the FWHM values of our dropouts to these statistics. A dropout is deemed a point source if its FWHM in at least one band is within 5σ of the average in this band. As an extended source can never have an FWHM of a point source, this one-band requirement will not include non-point sources. We did not impose this requirement to all bands where the object is detected, as it would be too stringent. First of all, a point source could have a large FWHM measured when lacking sufficient S/N. Second, the drizzle algorithm (Fruchter & Hook 2002) used by the JWST image stacking routine does not strictly preserve the source FWHM (Fruchter 2011). Therefore, if a source has a pointlike FWHM in one band, it is safe to conclude that it is a point source.

The above criteria identify six point sources among the 60 F150W dropouts of Y23. Figure 1 shows their six-band image stamps as well as the Gaussian profile fitting results in the relevant bands. Five of them have F200W FWHM values sufficient for our point-source criteria, among which three also meet the criteria in F277W. The other one satisfies the criteria in F277W. Among the 15 F200W dropouts of Y23, two are identified as point sources. Their image stamps and the profile fitting results are shown in Figure 2. Both of them have F277W and F356W images that satisfy the criteria, one of which also satisfies the criteria in F444W (but this fitting result is not shown). One of the 12 Y23 F277W dropouts meets the criteria in both F356W and F444W, which is shown in Figure 3. Finally, the only object in the $m_{444} \leqslant 29.0$ mag F356W dropout sample satisfies the criteria in F444W, which is shown in Figure 4. The catalog of all these point-source dropouts is given in Table 1. We note that the magnitudes of these objects are slightly different from those quoted in Y23, because we carried out photometry using the new mosaics based on the updated flux calibration. Following Y23, the matched-aperture photometry was done by running SExtractor (Bertin & Arnouts 1996) in the dual-image mode to ensure accurate color measurements. For the F356W dropout, the detection image was the F444W stack. For all other objects, the detection image was the F356W stack. The background was estimated locally. The isophotal magnitudes "MAG_ISO" were adopted; as argued in Y23, the sources of our interest are small enough in the images such that the MAG_ISO apertures include nearly all the source flux while minimizing the background noise.

3. Supernova Interpretation

Our current exercise is to fit the SEDs of these point-source dropouts with spectral sequences of Type Ia supernovae (SNe Ia) and typical Type IIP supernovae (SNe IIP) templates. The SNe Ia templates are derived from the SALT3-NIR models of Pierel et al. (2018, 2022), while those of SNe IIP are based on Peter Nugent's templates (Gilliland et al. 1999). We have applied simple power-law extrapolations in the wavelength ranges not covered by these templates.

For each object, the following χ^2 is minimized:

$$\chi^2(m_0, z, t, \boldsymbol{p}) = \sum_{\lambda_i} \frac{(m_{\rm obs}(\lambda_i) - m_{\rm SED}(\lambda_i; z, t, \boldsymbol{p}) + m_0)^2}{\sigma^2_{\rm obs}(\lambda_i)} + \left(\frac{m_0}{\delta m_0}\right)^2,$$

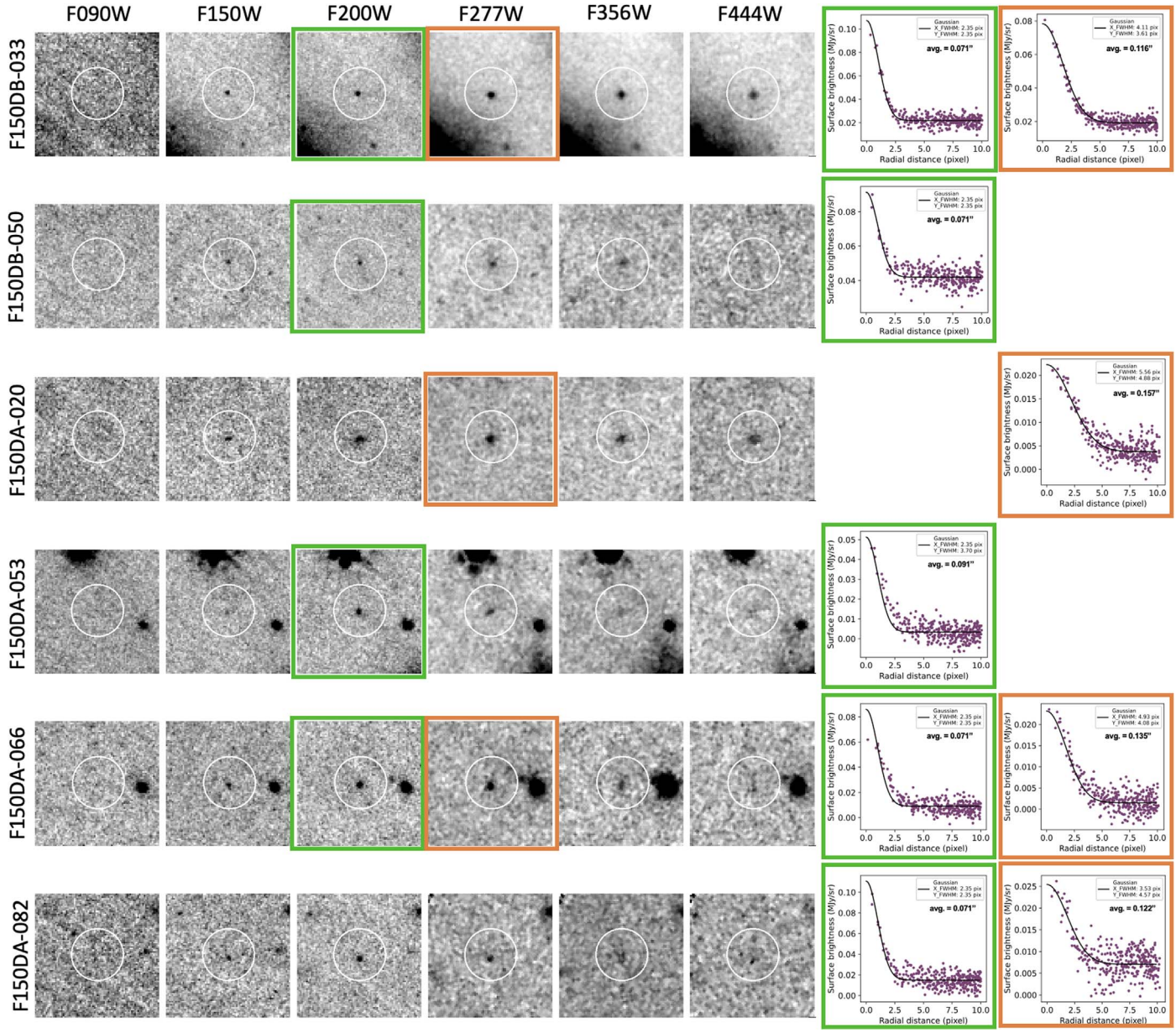

Figure 1. Six-band image stamps and profile fitting results of the six point-source F150W dropouts in the Y23 sample (among 60 in total). The image stamps ($2\farcs4 \times 2\farcs4$ in size) are based on the 30 mas stacks, and the white circles ($0\farcs5$ in radius) are centered on the dropouts. The dropout "short IDs" (as in Y23) are labeled to left, while the passbands are labeled on top. The images used for the 2D Gaussian profile fitting are outlined by the green (for F200W) and orange (for F277W) boxes. The corresponding fitting results are shown in the boxes to right, outlined by the same colors. The legends show the image FWHM values in units of pixels along both axes, and the averages in units of arcseconds are also labeled.

where m_0, z, and t are the magnitude offset, redshift, and time from the optical peak of the templates, respectively; $\boldsymbol{p}$ denotes either the SALT3 (x_1, c) parameters for the SNe Ia templates or the reddening $E(B-V)$ for the SNe IIP templates; $m_{\rm obs}$ and $\sigma_{\rm obs}$ are the observed magnitudes and errors; and $m_{\rm SED}$ represents the template SED used for the fits, with δm_0 characterizing the magnitude dispersion of the given template. The second term on the right-hand side of the above equation represents a penalty term for the cases where the observations have significant deviations from the absolute magnitudes of the SEDs.

In such SNe Ia fits, there are four free parameters for each object: the time of the B-band maximum, the magnitude offset from the peak B-band maximum (a positive offset value means that the template is fainter than the observed SED), and the SALT parameters x_1 and c that control the subtypes of SNe Ia. As we are not fitting cosmological distances, we simply adopt the B-band absolute magnitude of an SN Ia with $x_1 = 0$ and $c = 0$ to be ~ -19.3 mag, which corresponds to a Hubble constant of ~ 71 km s^{-1} Mpc^{-1}. The allowed ranges of x_1 and c are $[-3, 3]$ and $[-0.3, 0.3]$, respectively, which capture all the SN Ia light curves analyzed in Pierel et al. (2022). We set δm_0 loosely to 1.0 mag to calculate the penalty term that disfavors large magnitude offset from the templates. For SNe IIP, we assume the absolute B-band magnitudes of $M_{\rm B} = -18$ mag at the optical maximum with a scatter of $\delta m_0 = 3.0$ mag.

The results are shown in Figure 5 for SNe Ia and Figure 6 for SNe II, respectively. Most candidates agree with either type; some of them agree with both but with different best-fit

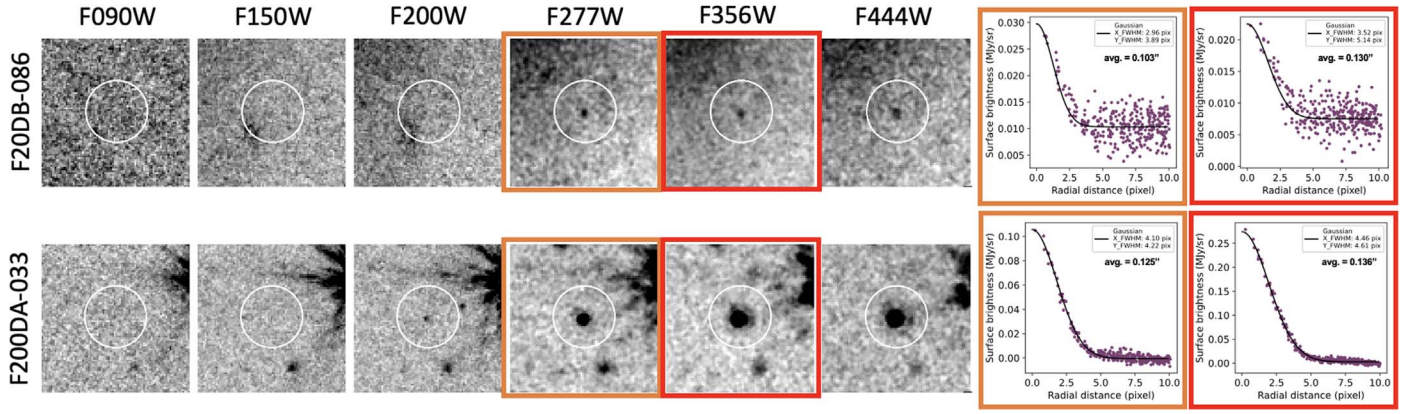

Figure 2. Similar to Figure 1, but for the two point-source F200W dropouts in the Y23 sample (among 15 in total). The images used for the profile fitting are outlined by the orange (for F277W) and red (for F356W) boxes. F200DA-033 also satisfies the point-source criteria in F444W, which is not shown due to the limited space.

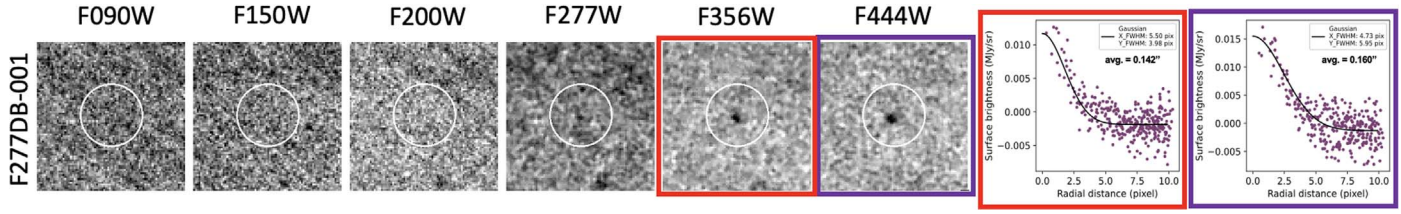

Figure 3. Similar to Figure 1, but for the one point-source F277W dropout in the Y23 sample (among 12 in total). The images used for the profile fitting are outlined by the red (for F356W) and purple (for F444W) boxes.

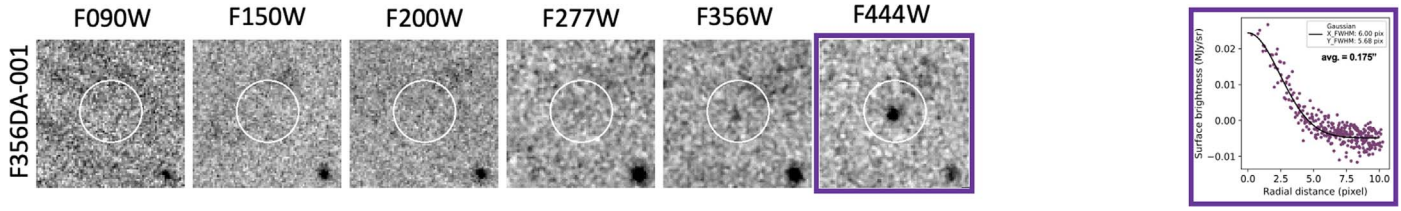

Figure 4. Similar to Figure 1, but for the only object in the new F356W dropout sample truncated at $m_{444} \leqslant 29.0$ mag. The F444W image (outlined by the purple box) of this object satisfies our point-source criteria.

redshifts and phases. Specifically, these objects have good fits with SNe Ia and/or SNe IIP: F150DA-020, F150DA-053, F150DB-050, F200DB-086, and F277DB-001. F150DA-033 is consistent with an SN IIP, but with a large magnitude offset that cannot be explained by gravitational magnification by the foreground cluster. Likewise, the reddest object, F356DA-001, if it is a transient, cannot be an SN Ia; it can be fitted with the adopted SN IIP SEDs only if the object is at $z \gtrsim 10$.

We note two points regarding these fits. First, the magnitude offset is left as a free parameter in the fitting (even for SNe Ia), and the range of the absolute magnitude distribution we have adopted in our fits is broader than normally observed in the local universe. This can be justified by the uncertainties introduced by gravitational lensing magnification and/or interstellar dust extinction. The objects in module B (indicated by "B" in their SIDs) could be amplified by the gravitational lensing effect due to the cluster.[5] The SALT c parameter corrects both the intrinsic SN color and the dust extinction. As these are largely based on the observations of local SNe, it is unclear whether the same corrections are applicable over the redshift range considered here (for example, the possible interstellar dust extinction at $z > 6$ is highly uncertain). This is exacerbated by the fact that most of our sources only have positive detections in a few bands, and the wavelength range is not broad enough to tightly constrain the interstellar dust extinction. In future works with more data (e.g., with new observations at different epochs), an additional penalty term based on the lensing and reddening probabilities can be added to the χ^2 calculation to better account for these effects.

Another point is regarding the χ^2 values. For many of these fits, the χ^2 values are less than the degrees of freedom (2 and 3 for SNe Ia and SNe IIP, respectively). This is mainly due to the null detections in the blue bands: while they are critical in constraining the redshifts of the objects, they are treated as data points with very large errors, which lead to very small χ^2. In such cases, only the redshifts are constrained for a given template, and the data do not have enough power to constrain the phases and intrinsic properties of the SNe. This is shown in the inset contours (for example, see the cases for F277DB-001 and F356DA-001). Even with six bands, the single-epoch SEDs alone cannot distinguish most SNe Ia from SNe IIP (in fact, from any other types of SNe). For most candidates, both the SNe Ia and SNe IIP can provide satisfactory fits; the

[5] However, the amplification factors quoted in Y23 are not applicable here because these were calculated based on the assumption that they are at $z > 11$, and therefore these values cannot be used here directly for correction.

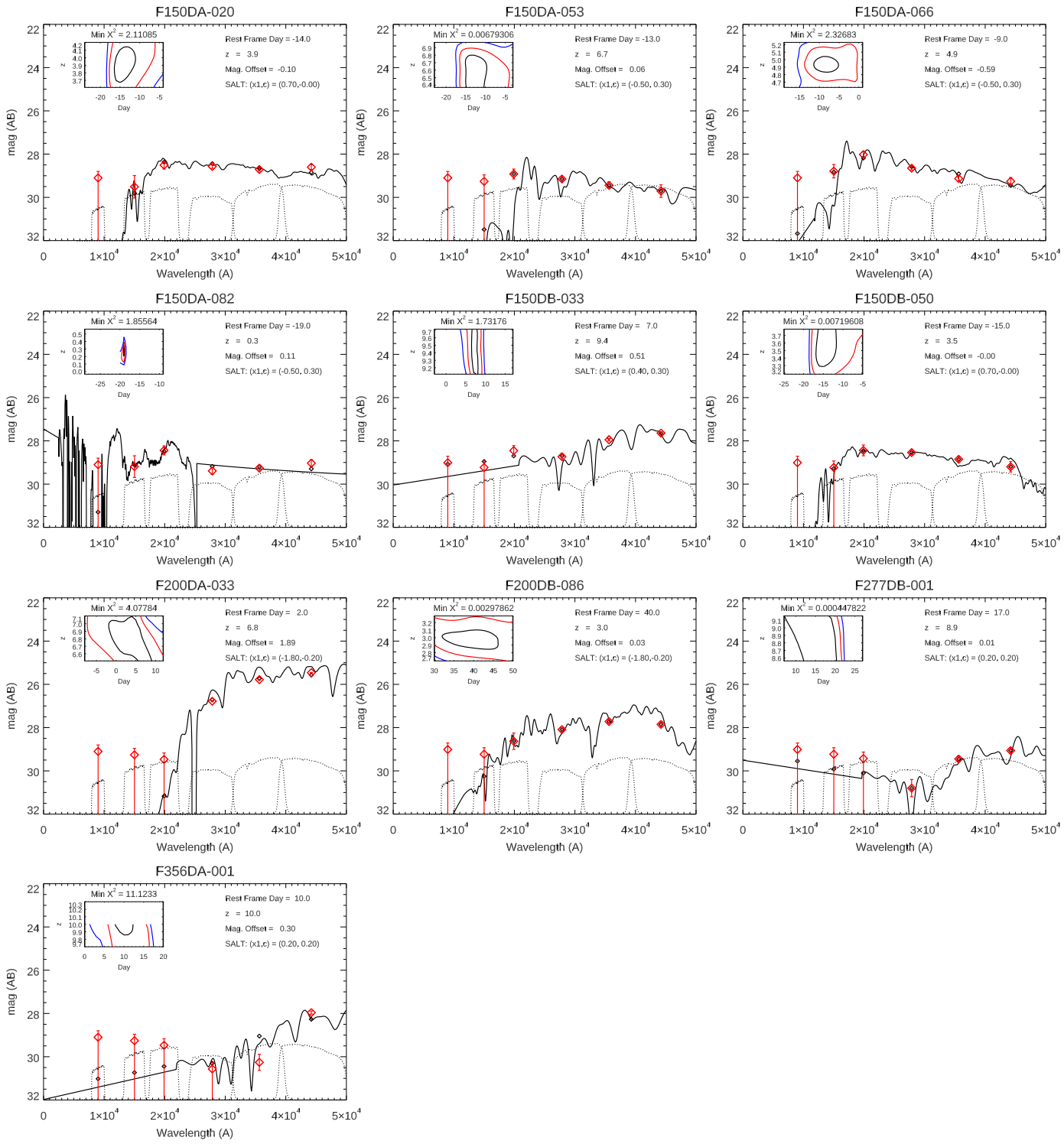

Figure 5. SED fitting results of the point-source dropouts using Type Ia supernova templates. The object IDs are given at the top of each panel. The red symbols show the photometry as in Table 1. The solid lines are the best-fit Type Ia SN templates, and the black diamonds are the synthesized magnitudes in the six NIRCam bands (indicated by the dotted lines in each panel). The legends show the time since the optical maximum (a negative value means the time before the B maximum) in the rest-frame days, the best-fit redshift, the magnitude offset from the best-fit model, and the SALT3NIR (x_1, c) parameters. Note that a positive magnitude offset means that observed SED is fainter than the template used, as defined by the equation in Section 3. The insets show how the redshift and time of SN are constrained, with the black, red, and blue contours indicating the 1σ, 2σ, and 3σ levels, respectively.

exceptions are F200DA-033 and F356DA-001, which strongly favor the SN IIP identifications. This is because the redshifts and other template parameters are all correlated quantities in the fits. As the result, an SN Ia at a given phase and redshift may be equally well fit by an SN IIP at a different phase and a different redshift. Only at some certain phases are the SEDs different enough that their spectral types can be robustly identified based on single-epoch photometry. Had we had multiepoch observations, the SN types and the phases would be much better constrained.

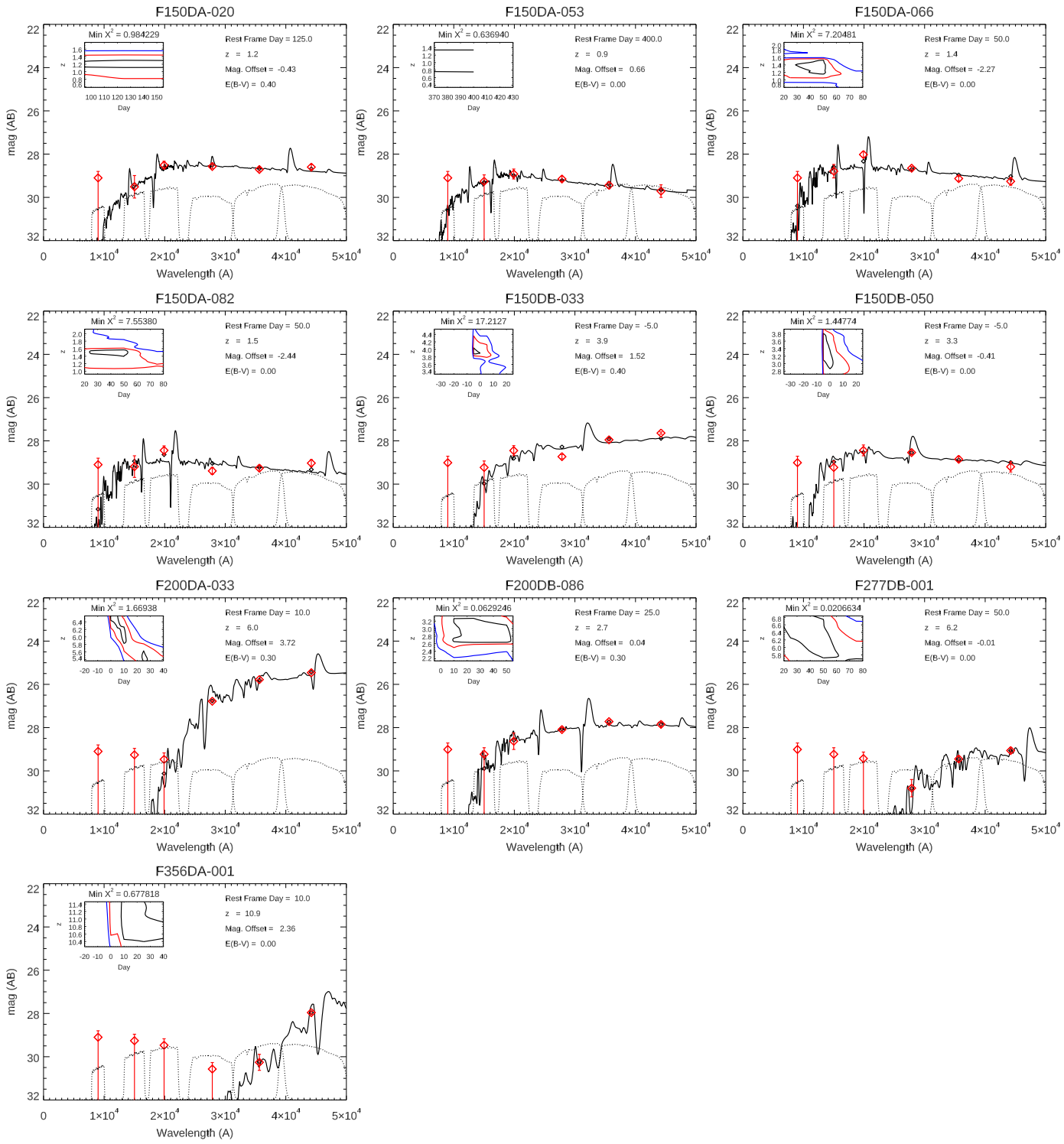

Figure 6. Similar to Figure 5, but using Type IIP supernova templates and with the best-fit $E(B-V)$ value shown in the legend.

4. Discussions

4.1. Implications of the Supernova Interpretation

While our result suggests that the point-source dropouts are consistent with being SNe, by no means do they prove that they are. One argument against this interpretation is the lack of obvious host galaxies associated with these sources. If these are SNe, this implies that they are in very diffuse, faint galaxies that are not detected by the current NIRCam data. SNe Ia in extremely faint galaxies have been observed by the Hubble Space Telescope, and it has been suggested that SNe Ia rates may be enhanced in dwarf galaxies or globular clusters (Graham et al. 2015). Therefore, it is not unreasonable that our objects are hostless SNe. If true, this may imply that hostless SNe dominate the SN production at $z \sim 3$. They can have a profound impact on the metal enrichment of the

Table 1
Catalog of Point-source Dropouts

ID	Short ID	m_{090}	m_{150}	m_{200}	m_{277}	m_{356}	m_{444}
F150DB J072330.55-732733.12	F150DB-033	>29.01	>29.23	28.45 ± 0.23	28.73 ± 0.10	27.95 ± 0.05	27.64 ± 0.05
F150DB J072324.58-732715.08	F150DB-050	>29.01	>29.23	28.44 ± 0.25	28.54 ± 0.10	28.85 ± 0.12	29.20 ± 0.24
F150DA J072255.88-732917.48	F150DA-020	>29.10	29.51 ± 0.52	28.51 ± 0.18	28.57 ± 0.09	28.71 ± 0.08	28.60 ± 0.11
F150DA J072232.48-732833.23	F150DA-053	>29.10	>29.26	28.92 ± 0.23	29.15 ± 0.12	29.44 ± 0.15	29.71 ± 0.29
F150DA J072239.62-732812.19	F150DA-066	>29.10	28.79 ± 0.31	28.02 ± 0.13	28.65 ± 0.08	29.13 ± 0.11	29.26 ± 0.18
F150DA J072252.78-732741.93	F150DA-082	>29.10	29.19 ± 0.50	28.44 ± 0.21	29.39 ± 0.16	29.26 ± 0.13	29.03 ± 0.16
F200DB J072306.42-732719.88	F200DB-086	>29.01	>29.23	28.63 ± 0.38	28.09 ± 0.09	27.72 ± 0.07	27.85 ± 0.11
F200DA J072243.92-732915.78	F200DA-033	>29.10	>29.26	>29.47	26.78 ± 0.03	25.78 ± 0.01	25.46 ± 0.01
F277DB J072317.55-732825.26	F277DB-001	>29.01	>29.23	>29.43	30.80 ± 0.40	29.45 ± 0.12	29.06 ± 0.12
F356DA J072233.26-732911.14	F356DA-001	>29.10	>29.26	>29.47	>30.57	30.26 ± 0.37	27.96 ± 0.07

Note. The first nine objects are from the dropout sample of Y23, but with the photometry updated using the new calibrations as in the CRDS context jwst_1008.pmap. The last object is an F356W dropout from this current work. The nomenclature follows Y23's catalog table.

intergalactic medium because their ejecta can escape freely into the intergalactic medium. This in fact corroborates with the Chandra X-ray observations of the intracluster medium, which shows an early metal enrichment of the intracluster medium (Mantz et al. 2017) as evidenced by a constant metallicity at large radii (0.5–1 r_{500}) from the cluster center[6] and a late-time increase in enrichment at intermediate radii (0.1–0.5 r_{500}).

Another concern is whether it is physically plausible to have so many SNe in such a small field. It is noteworthy that, at the depth of these JWST observations, a significant number of SNe Ia and even some of the bright SNe II to redshifts as high as $z \approx 6$ can be detected. By extrapolating the local rate of SNe Ia following the constraint of the global star formation history of the universe, one would expect to discover 2.5 ± 0.6 SNe Ia at $z \approx 2$–6 in a single NIRCam pointing at the depth of ∼30 mag (Wang et al. 2017; Regős & Vinkó 2019). The number of SNe II is comparable, although they only extend to a lower redshift range as they are generally less luminous. Therefore, one would expect a total of ∼5 SNe in one NIRCam field like what we study here. Given the uncertainty of the predictions, this is in broad agreement with the hypothesis that at least a large fraction of the point-source dropouts studied here are SNe.

4.2. Supernovae as Possible Contaminants in the z > 11 Candidate Galaxy Sample

Y23 cautioned that there could be some new types of contaminators in the $z > 11$ candidate search that were not encountered before. This current work shows that SNe could be one such type that should be considered if the candidate is pointlike. Taking the χ^2 at face value, the SNe templates provide better fits to these objects than in Y23. Such point-source dropouts are present in the 1.5–2.0 μm dropout sample of Yan et al. (2023a) as well, and likely also elsewhere. To effectively remove such contaminants, multiple-epoch imaging is probably the most efficient. Due to the time dilation at high redshifts ($z \gtrsim 3$ in this context), SNe will not necessarily manifest themselves as transients in the multiple-epoch observations. However, they can be singled out as variable objects.

Among the 10 point-source dropouts considered here, 9 are in the Y23 sample (it does not include any F356W dropouts) that has 87 objects in total. If these point sources are indeed SNe, the contamination rate due to SNe is only ∼10%. Therefore, the tension between the current NIRCam $z > 11$ candidates and the previously favored model predictions cannot be removed by resorting to this new type of contaminator; the non-point-source candidates cannot be explained in this way.

An interesting point is that a point-source F356W dropout will have to be at $z > 10$ if interpreted as an SN. This is because the rest-frame blue-end cutoff at ∼4000 Å occurring in F356W means that the redshift must be at $z > 10$. This is shown in both Figures 5 and 6 for object F350DA-001. As it takes time for a low-mass star to evolve to a white dwarf that is needed for an SN Ia, most likely an SN at such a high redshift cannot be an SN Ia but should be a core-collapse supernova. Therefore, ironically, finding point-source F356W dropouts and attributing them to SNe would still suggest that the global star formation rate density (GSFRD) at $z > 10$ must be much higher than what was previously favored. We will defer a more detailed calculation to a future paper.

For simplicity, we only consider SNe Ia and IIP in this work. However, we note that other types of SNe could also be used to explain such sources. These could include rarer types such as the hydrogen deficient SNe Ib/c, SNe with strong ejecta–circumstellar interaction (SNe IIn), and superluminous supernovae (SLSNe). The theoretically perceived pair-production supernovae (PPSNe) from zero-metallicity stars are also a possibility. Acquiring multiepoch data can enable further investigations on such scenarios.

5. Summary

In this work, we investigate the problem of the pointlike sources in the $z > 11$ candidate galaxy sample of Y23, which are unlikely Galactic brown dwarf stars. We find that such sources might indeed be new kinds of contaminators to high-z candidate samples: these could be SNe at various redshifts. This somewhat alleviates the tension but does not eliminate it, as there are plenty of non-point-source objects in the $z > 11$ candidate samples published to date. As a reference, the pointlike sources only constitute ∼10% of the Y23 sample.

On the other hand, this work shows that SNe at $z > 3$ might already have been detected in the NIRCam data and that they could be singled out using SED fitting to point-source dropouts at >1.5 μm. Finding SNe at $z > 3$ will have a series of important implications. Multiple-epoch NIRCam imaging is the most efficient way to test the SN hypothesis. Due to the time dilation and the high sensitivity of NIRCam, SNe at high redshifts most likely would show up as variable objects (but not necessarily as

[6] r_{500} is the radius at which the density is 500 times the mean density of the universe at the redshift of the cluster.

transients) in multiple-epoch NIRCam images. Such data would greatly improve the constraints on their redshifts and the elapsed time before/after the maximum. This will enable quick identifications of the most important SN candidates, e.g., SNe Ia at $z \approx 6$–10, for spectroscopic confirmation.

Finally, we remark that SNe Ia at such redshifts can be used to quantitatively constrain the systematic redshift evolution of the intrinsic properties of SNe Ia (Riess & Livio 2006; Lu et al. 2022) by incorporating explicit redshift-dependent light-curve shape and color corrections to SN Ia magnitudes.

All the JWST data used in this Letter can be found in MAST at doi:10.17909/7rjp-th98.

H.Y. acknowledges the partial support from the University of Missouri Research Council Grant URC-23-029. L.W. acknowledges support from the NSF through the project AST-1817099. L. H. acknowledges support from China Postdoctoral Science Foundation (grant No. 2022M723372) and the Jiangsu Funding Program for Excellent Postdoctoral Talent.

Appendix

To determine the point-source FWHM distributions, we used the methodology of the PSFEx tool (Bertin 2011). In the magnitude (SExtractor's MAG_AUTO) versus half-light radius (SExtractor's FLUX_RADIUS with PHOT_FLUXFRAC = 0.5) plot, point sources occupy a nearly vertical locus. This is shown in Figure A1 for our case in F200W as an example. The initial point sources were selected within this locus, with the additional constraints that they should have high S/N (SExtractor's SNR_WIN > 30.0) and be relatively round (ELLIPTICITY < 0.3). We ran PSFEx on these initial sources and measured the average FWHM after 5σ clipping. The module A (B) FWHM values and rms thus obtained are $0\farcs076 \pm 0\farcs004$, $0\farcs121 \pm 0\farcs005$, $0\farcs139 \pm 0\farcs004$, and $0\farcs161 \pm 0\farcs006$ ($0\farcs079 \pm 0\farcs006$, $0\farcs124 \pm 0\farcs007$, $0\farcs142 \pm 0\farcs005$, and $0\farcs164 \pm 0\farcs004$) in F200W, F277W, F356W, and F444W, respectively. The FWHM distribution of the retained point sources in F200W is shown in Figure A2 as an example.

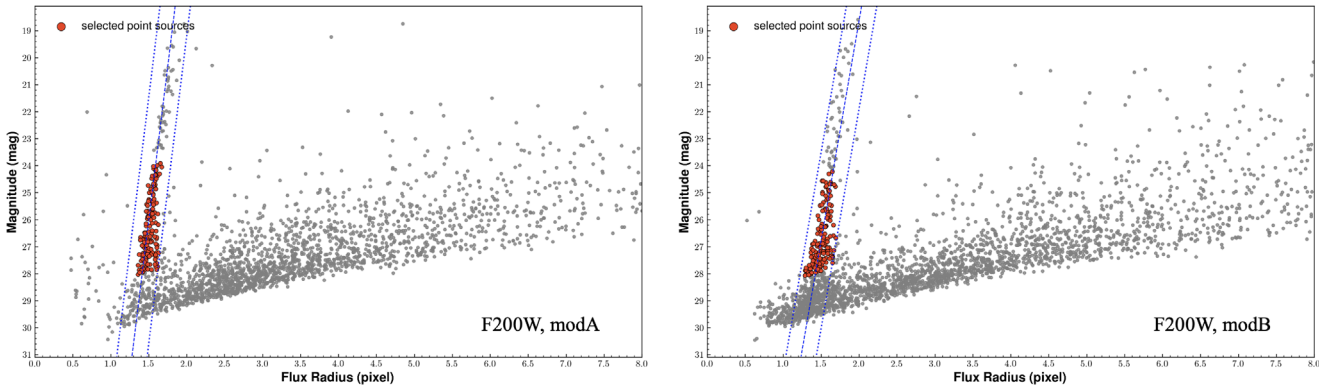

Figure A1. Selection of bright point sources to measure the FWHM distribution, using F200W as an example. The left panel is for module A and the right panel is for module B, respectively. The *y*-axis is the SExtractor MAG_AUTO magnitude, while the *x*-axis is the radius (in pixels; 30 mas pixel scale) of a circle aperture that contains half of the total flux. The point sources are within a narrow "belt" as outlined. The red dots are the sources retained for the statistics.

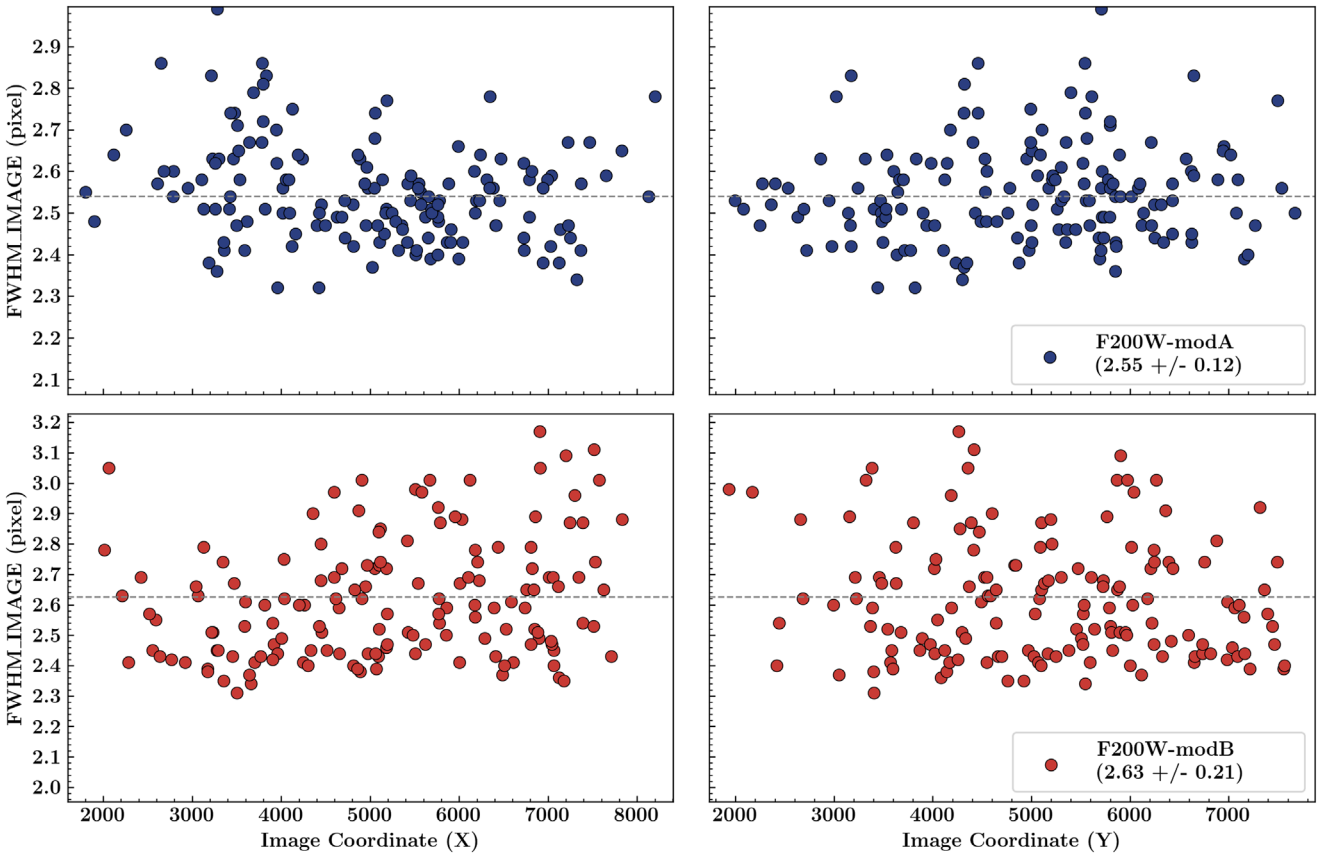

Figure A2. FWHM distribution of bright point sources as a function of image coordinates (*X* on the left and *Y* on the right, respectively). The case in F200W is shown here as an example. The top panels are for module A, and the bottom panels are for module B, respectively. The FWHM values are in pixels; the pixel scale is 30 mas.

ORCID iDs

Haojing Yan https://orcid.org/0000-0001-7592-7714
Lifan Wang https://orcid.org/0000-0001-7092-9374
Zhiyuan Ma https://orcid.org/0000-0003-3270-6844
Lei Hu https://orcid.org/0000-0001-7201-1938

References

Adams, N. J., Conselice, C. J., Ferreira, L., et al. 2023, MNRAS, 518, 4755
Atek, H., Shuntov, M., Furtak, L. J., et al. 2023, MNRAS, 519, 1201
Behroozi, P., Conroy, C., Wechsler, R. H., et al. 2020, MNRAS, 499, 5702
Bertin, E. 2011, in ASP Conf. Ser. 442, Astronomical Data Analysis Software and Systems XX, ed. I. N. Evans et al. (San Francisco, CA: ASP), 435
Bertin, E., & Arnouts, S. 1996, A&AS, 117, 393
Bouwens, R. J., Stefanon, M., Brammer, G., et al. 2022, arXiv:2211.02607
Castellano, M., Fontana, A., Treu, T., et al. 2022, ApJL, 938, L15
Donnan, C. T., McLeod, D. J., Dunlop, J. S., et al. 2023, MNRAS, 518, 6011
Finkelstein, S. L., Bagley, M. B., Haro, P. A., et al. 2022, ApJL, 940, L55
Fruchter, A. S. 2011, PASP, 123, 497
Fruchter, A. S., & Hook, R. N. 2002, PASP, 114, 144
Gilliland, R. L., Nugent, P. E., & Phillips, M. M. 1999, ApJ, 521, 30
Graham, M. L., Sand, D. J., Zaritsky, D., & Pritchet, C. J. 2015, ApJ, 807, 83
Harikane, Y., Ouchi, M., Oguri, M., et al. 2022, ApJS, 265, 5
Lu, J., Wang, L., Chen, X., et al. 2022, ApJ, 941, 71
Mantz, A. B., Allen, S. W., Morris, R. G., et al. 2017, MNRAS, 472, 2877
Naidu, R. P., Oesch, P. A., van Dokkum, P., et al. 2022, ApJL, 940, L14
Pierel, J. D. R., Jones, D. O., Kenworthy, W. D., et al. 2022, ApJ, 939, 11
Pierel, J. D. R., Rodney, S., Avelino, A., et al. 2018, PASP, 130, 114504
Pontoppidan, K., Blome, C., Braun, H., et al. 2022, ApJL, 936, L14
Regős, E., & Vinkó, J. 2019, ApJ, 874, 158
Riess, A. G., & Livio, M. 2006, ApJ, 648, 884
Rodighiero, G., Bisigello, L., Iani, E., et al. 2023, MNRAS, 518, L19
Steidel, C. C., Pettini, M., & Hamilton, D. 1995, AJ, 110, 2519
Vogelsberger, M., Nelson, D., Pillepich, A., et al. 2020, MNRAS, 492, 5167
Wang, L., Baade, D., Baron, E., et al. 2017, arXiv:1710.07005
Yan, H., Cohen, S. H., Windhorst, R. A., et al. 2023a, ApJL, 942, L8
Yan, H., Ma, Z., Ling, C., Cheng, C., & Huang, J.-S. 2023b, ApJL, 942, L9